# Polarization-modulated multi-directional photothermal actuators

Zhiwei Li, Zuyang Ye, Lili Han, Qingsong Fan, Chaolumen Wu, Deng Ding, Huolin L. Xin, Nosang Vincent Myung, and Yadong Yin

Dr. Z. W. Li, Z. Y. Ye, Q. S. Fan, C. L. M. Wu, Prof. Y. Yin

Department of Chemistry, Center for Catalysis, University of California Riverside, Riverside, California 92521, United States

Email: <u>yadong.yin@ucr.edu</u> D. Ding, Prof. N. V. Myung

Department of Chemical and Environmental Engineering, University of California Riverside, Riverside, California 92521, United States

Email: <u>myung@engr.ucr.edu</u> Dr. L. L. Han, Prof. H. L. Xin

Department of Physics and Astronomy, University of California-Irvine, Irvine, California 92697, United States

Keywords: Plasmonic nanorods, templating synthesis, magnetic alignment, photothermal actuators, multi-directional robots

#### Abstract:

Photothermal actuators have attracted increasing attention due to their ability to convert light energy into mechanical deformation and locomotion. This work reports a free-standing, multi-directional photothermal robot that can walk along a pre-designed pathway by modulating laser polarization and on-off switching. Magnetic-plasmonic hybrid Fe<sub>3</sub>O<sub>4</sub>/Ag nanorods are synthesized using an unconventional templating approach. The coupled magnetic and plasmonic anisotropy allows the control of the rod orientation, plasmonic excitation, and photothermal conversion by simply applying a magnetic field. Once the rods are fixed with desirable orientations in a bimorph actuator by magnetic field-assisted lithography, the bending of the actuator can be controlled by switching laser polarization. A bipedal robot is created by coupling the rod orientation with the alternating actuation of its two legs. Irradiating the robot by a laser with alternating or fixed polarization synergistically results in basic moving (backward and

forward) and turning (including left-, right-, and U-turn), respectively. A complex walk along pre-designed pathways can be potentially programmed by combining the moving and turning modes of the robots. This strategy provides an alternative driving mechanism for preparing functional soft robots, thus breaking through the limitations in the existing systems in terms of light sources and actuation manners.

Photothermal soft actuators or robots rely on the photothermal effects of light-absorbing materials, such as carbon materials, [1] plasmonic nanostructures, [2] and organic dyes [3] for converting light energy to mechanical deformation and locomotion. Compared with soft actuators that are powered by other stimuli, [4] including electricity, [5] magnetic field, [6] solvent, [7] moisture, [8] salt, [9] and heat, [10] photothermal robots take advantage of light as a clean and safe energy source for precise, remote, and fast mechanical actuation. [1b, 11] Compared with photochemical actuation and optical tweezers, light-absorbing materials can be incorporated into various functional matrices to perform the desired mechanical work, thereby providing more flexibility in actuator design and more opportunities for practical applications. [12] Over the past decade, photothermal actuators are of particular interest and have been widely exploited in biomimetic robots, tissue engineering, biomedicine, and artificial intelligent systems. [13]

A typical photothermal actuating system comprises three components: light-absorbing materials for efficient photothermal conversion, thermally responsive layers for volume expansion, phase change, or molecular desorption, as well as passive layers.<sup>[12c, 14]</sup> In some cases, the light-absorbing materials also serve as active or passive layers.<sup>[15]</sup> This simple design of materials represents an open platform for achieving some basic mechanical deformations, including bending, twisting, and rotation.<sup>[13b]</sup> Of more significant challenges is to transform this shape-

morphing into well-controlled multimodal locomotion to achieve functions desired for different demands. Bimorph photothermal actuators can crawl on a substrate with a sawtooth-featured surface in one direction, representing an effective approach toward directional locomotion. [2a, 16] Bio-inspired soft robots are more often designed into asymmetric shapes to mimic specific movements of natural creatures.<sup>[17]</sup> These strategies have advantages of easy fabrication, simple actuation, and a low requirement on light source yet are limited to providing one-way movement, which makes it challenging to realize the bionic functionalities. Extending the movement degrees of freedom can be achieved by precisely controlling the irradiation position or the scanning direction of light.<sup>[18]</sup> A few advanced working mechanisms involve the wavelength-dependent photothermal conversion and selective actuation of specific domains of hierarchical architectures so that multi-directional move can be produced reversibly. Liquid crystal elastomers, for example, contain different light-absorbing dyes can perform multi-directional move by using three lasers at the specific wavelength.<sup>[19]</sup> These methods require complicated modulation of light source to induce asymmetric shape deformation and directional move or on-demand turning. In addition, the complicated fabrication process, demanding actuation procedure, and limited choice of materials pose additional restrictions on their practical applications.

While modulating light polarization has the potential for controlling the physical properties of nanostructures, [14d, 20] its application in developing soft actuators capable of multiplex movements has not been fully explored due to the lack of processes and materials for efficient orientational control and photothermal conversion. Here, we report a free-standing, multi-directional photothermal actuator that can be simply actuated by controlling the polarization of a single laser beam. This bipedal robot takes advantage of the selective excitation of plasmonic rods when rod orientation can be conveniently controlled. To this end, we use an unconventional

templating approach to directly synthesize hybrid Fe<sub>3</sub>O<sub>4</sub>/Ag nanorods with coupled magnetic-plasmonic anisotropy. Relying on the unique Janus structure, the orientation and physical properties of the rods can be actively tuned by applying a magnetic field. Further fixing the orientation of the rods in the polymer matrix enables selective photothermal conversion and bending of film actuators. As a proof-of-concept, a bipedal robot was prepared by magnetically aligning the hybrid Fe<sub>3</sub>O<sub>4</sub>/Ag nanorods with orthogonal collective orientation in its two legs. Modulating the laser polarization during irradiation can selectively actuate the two legs on demand, which synergistically drives the locomotion of the robot. For example, straight walking or turning can be achieved by irradiating the robot with a laser of alternative or fixed polarization, respectively. By programming the two irradiation modes, the free-standing robot can walk along any pre-designed pathway using a laser beam.

The hybrid or Janus nanorods were synthesized by an unconventional templating approach as reported previously. [2a, 21] Briefly, magnetic nanorods (110 nm×20 nm) are used as an initial template. [22] Au seeds (~2 nm, denoted as Aus) were attached to their surface through electrostatic interactions (Figure S1, Supporting Information). [23] Ag was chosen as the light-absorbing material because Ag has a much lower cost, higher abundance, stronger plasmonic activities, and higher photothermal conversion efficiency compared with Au. [24] Besides, Ag nanorods have a transverse mode at short wavelength, and the large separation of the two resonance peaks may facilitate the polarization-selective photothermal conversion and actuation. [25] For growing uniform Ag nanorods, resorcinol is used as a reducing agent to avoid free nucleation because its weak reducing power can keep the Ag monomers below the nucleation concentration limit. [26] Also, it maintains the continuous Ag deposition by avoiding the stepwise addition or slow injection of Ag precursors. [27] The reaction temperature was raised

to 80 °C, which could enhance the Ostwald ripening at the initial stage of the reaction. Consequently, many small Au seeds were oxidized by oxygen and dissolved in the reaction (Figure S2, Supporting Information). We observe an inhomogeneous growth of Ag in the templates, which is largely ascribed to the strong coordination between Ag<sup>+</sup> and trapped NH<sub>4</sub><sup>+</sup> and the slow diffusion of Ag<sup>+</sup> through the resorcinol-formaldehyde (RF) shells. [28] If RF shells are etched by NaOH, the fast Ag<sup>+</sup> diffusion produces multiple large Ag grains (Figure S3, Supporting Information). This comparison underpins the important role of RF shells in regulating the growing kinetics: the slow diffusion of Ag<sup>+</sup> from the reaction solution to the inner gap retards the Ag growth, prolongs the Ostwald ripening process, and is responsible for the growth of Ag on limited seeds into high-quality rods (Figure S4, Supporting Information).

The final hybrid Fe<sub>3</sub>O<sub>4</sub>/Ag nanorods are shown in **Figure 1**a with uniform morphology and a smooth surface. Their two peaks at 410 nm and 920 nm are well separated with comparable intensity (Fig. S5, Supporting Information). The high-resolution TEM (HR-TEM) image in Figure S6 demonstrates a polycrystalline nature of Ag rods with a clear crystal boundary between the (111) facets. Figure S7 shows that the elemental signals of Ag overlap with signals of Fe, which confirms the hybrid structure of Fe<sub>3</sub>O<sub>4</sub> and Ag nanorods in a parallel alignment. The fine structure of the hybrid rods is further resolved by electron tomography. Figure 1b is a 3D reconstructed hybrid nanorod with a side-by-side configuration that is completely wrapped by an RF shell (See Supporting Video 1 for the 3D view of the rod). By reconstructing horizontal slices at three vertical positions, the rod position, morphology, and Fe<sub>3</sub>O<sub>4</sub>-Ag interface can be observed (Figure 1c). The first, second, and third cross-sections at the corresponding 1/4, 1/2, and 3/4 of the rod thickness are shown in Figure 1d. Notably, due to the templating effect, the Fe<sub>3</sub>O<sub>4</sub> rod creates a concave defect in the Ag rod with a smooth, clear domain boundary between them

(Supporting Video 2). The absorption peak and aspect ratio of Ag rods can be controlled by changing the silica thickness. When a thin silica layer (~5 nm) was used, the peak of longitudinal mode redshifted to 955 nm, and the templates produced thin Ag rods with a large aspect ratio (Figure S8, Supporting Information). Meanwhile, we observe a new peak at ~550 nm, largely because of the surface concavity of Ag rods, which induces a new concave peak. [21] Our thermal treatment on the hybrid rods demonstrates the perfect thermostability of Ag rods (Figure S9, Supporting Information). The strong coordination between Ag and trapped NH4<sup>+</sup> in RF shell is one possible reason for this enhanced stability.

The magnetic Fe<sub>3</sub>O<sub>4</sub> rod has a unique shape anisotropy with preferential parallel alignment to a magnetic field to minimize magnetic potential energy. [29] The orientation of the neighboring Ag rods can be controlled by applying a magnet because of the coupled magnetic-plasmonic anisotropy.<sup>[30]</sup> Measuring the rods extinction under z-polarized light provides a quantitative excitation-orientation correlation (Figure S10, Supporting Information). As the rods were magnetically aligned from  $|0^{\circ}\rangle$  to  $|90^{\circ}\rangle$  (Figure 1e), we observed a gradual suppression of longitudinal mode and enhancement of transverse mode, whose excitation can be described by  $\cos^2\Theta$  and  $\sin^2\Theta$ , respectively ( $\Theta$  is the angle between rod orientation and polarization). These observations predict that it is possible to control the photothermal conversion of hybrid rods using the same magnetic orientation control. To verify this hypothesis, we first measured the temperature of rod dispersion during 450-nm laser irradiation while applying a magnetic field to control their collective orientation. In Figure 1f,  $\Delta T$  is larger or smaller than that measured under the absence of a magnetic field when a parallel ( $|0^{\circ}\rangle$ .) or perpendicular ( $|90^{\circ}\rangle$ .) field was applied, respectively. The different photothermal property is consistent with the selective excitation of the longitudinal mode. For example, at  $|0^{\circ}\rangle$ , the parallel alignment to laser polarization only excites

the longitudinal mode, and therefore  $\Delta T$  is higher than other configurations. The orientation-dependent photothermal conversion is similar in a solid polymer film. As shown in Figure 1g and 1h, the  $\Delta T$  was higher when only transverse mode (conditions ii and iii) was excited by a 450-nm laser. The results are consistent with our previous analysis and prove that, in solid films, the photothermal conversion of the collectively aligned rods can be controlled by changing the laser polarization. Compared with previous efforts in exploiting the orientation-dependent optical properties of nanomaterials, [20b, 31] the magnetic-plasmonic hybrid structures and the magnetic alignment strategy presented in this work demonstrate significant advantages of fast, revisable, remote, and accurate control over the orientation and physical properties of the anisotropic nanostructures.

To demonstrate the polarization-dependent actuation, we prepared a simple actuator using the different coefficients of thermal expansion (CTE) between polydimethylsiloxane (PDMS) and polyimide (PI).<sup>[32]</sup> There is a middle polyacrylamide (PAM) layer embedded with well-aligned Fe<sub>3</sub>O<sub>4</sub>/Ag rods, which serve as a photothermal converter (Figure 2a). This layer facilitates the magnetic alignment of hybrid nanorods during lithography because the polymerization of acrylamide occurs in an aqueous phase, where the hydrophilic rods can disperse well. Under laser irradiation, light energy is converted into heat by the embedded rods, which is simultaneously transferred to the neighboring PDMS and PI layers. Because PDMS has a much higher CTE than PI, the actuator exhibits a bending induced by higher volume expansion of PDMS. To verify the hypothesized polarization-modulated actuation, we prepared a two-leg actuator for parallel comparison. Fe<sub>3</sub>O<sub>4</sub>-Ag rods were aligned along the y- and x-axis in the right and left legs, respectively (Figure 2b). Under the irradiation of an x-polarized (|x><x|), 450-nm laser, only the transverse mode of the rods in the right leg is excited, producing selective bending

(Figure 2c). Therefore, in the experiment, the right leg bent much more than did the left leg (top panel in Figure 2d). The bending angle after 20-s irradiation was  $\sim$ 3.5-fold higher (Figure 2e). When the actuating laser was z-polarized, the transverse mode of rods in both legs was excited, leading to similar temperature changes as well as the same degree of bending. The polarization-selective actuation was further confirmed by the real-time angular velocity ( $\omega$ ) of the film actuators. Under the x-polarized light,  $\omega$  of the right leg approached the maximum speed of  $\sim$ 8°/s and then decreased gradually until the equilibrium position ( $\omega$ =0). In contrast,  $\omega$  of the left leg exhibited relatively small magnitude under the same light illumination. If a z-polarized light was used, the magnitude and decay of  $\omega$  were comparable in the two legs due to the simultaneous excitation of transverse modes. These results clearly show the excellent performance of the magnetic alignment strategy in achieving polarization-modulated actuation, which sets the stage ready for designing functional actuators and robots.

Based on the two-leg structures, we further propose a bipedal robot to demonstrate the polarization-modulated, multi-directional locomotion (Figure S12, Supporting Information). In this design, Fe<sub>3</sub>O<sub>4</sub>/Ag rods were magnetically aligned along the z- and x-axis in the right and left legs, respectively (**Figure 3**a). This specific design enables flexible, selective, and on-demand actuation of the two legs to form synergistic locomotion of the robot by controlling the laser polarization. As illustrated in Figure 3b, forward robot walking can be directly achieved by switching the polarization between |x><x| and |z><z|. At |x><x|, only the rods' transverse mode in the right leg was excited. Therefore, the right leg bends forward while the left leg, in principle, remains almost stationary (step I). Turning off the laser will terminate the photothermal conversion so that the right leg tends to recover its original plain form. Due to the specific shape of the feet, the right leg meanwhile experienced more friction than the left leg, which drives the

first-step forward-movement ( $\Delta L_R$ ) of the robot (step II). Similarly, when the robot was irradiated by z-polarized light, the rods in the left leg were excited, which selectively actuated the left leg (step III) and induced the second step of forward-movement ( $\Delta L_L$ ) during the following relaxation (step IV). This consequence of events is directly confirmed by the pictures shown in Figure 3c and Supporting video 3. Switching laser from |x><x| to |z><z| actuated the right- and left-leg bending, which constitutes one cycle of forward-movement. A quantitative analysis of these actuation processes helps to correlate the local leg deformation with the robot locomotion. As shown in Figures 3d and 3e, the bending angle in the polarization-matched leg is  $\sim$ 3 times higher than that in a nonmatched leg. The onset of laser on-off (25 s per cycle with 13 s and 12 s for light on and off, respectively) propels the robot forward at a step of  $\sim$ 1 mm and an apparent speed of  $\sim$ 2.8 mm/s. A continuous, steady forward movement can be implemented by switching between |x><x| and |z><z|, which is responsible for the alternating actuation of two legs. In Figure 3f, the real-time position mapping of the two legs suggests a linear alternating forward movement.

With the same design principle, we further demonstrate the on-demand turning of the robot. **Figure 4**a illustrates the force analysis of turning locomotion under laser illumination. At  $|z\sim z|$ , the left leg experiences associated backward friction (f<sub>L</sub>) due to its forward bending. When approaching the photothermal equilibrium, the left-leg bending, to some extent, induces a weak bending in the right leg through the strengthened robot body. For releasing the bending strain, the right leg tends to move backward, thus creating forward friction (f<sub>R</sub>) that is opposite to and also weaker than f<sub>L</sub>. This pair force works simultaneously to create a counterclockwise torque ( $\tau_L$ ) so that the robot turns left (the top view in Figure 4b). Simply repeating the irradiation of z-polarized light rotates the robot leftward gradually. One irradiation cycle produced ~15° rotation,

with 3 and 6 cycles for 45° and 90° turning, respectively (Supporting Video 4). Similarly, if laser polarization was switched to |x><x|, there exists a clockwise torque ( $\tau_R$ ) (Figure 4c). The robot gradually rotated rightward with a step of 15° (Figure 4d and Supporting Video 5). Notably, turning leftward (Figure 4e) or rightward (Figure 4f) is continuously driven by z- or x-polarized laser irradiation (22 s per cycle with both 11 s for light on and off), respectively, which is different from the alternating onset of the two polarization in forward-movement. Such the bending-relaxation cycles correlate with the smooth turning of the robot at an apparent rate of  $\sim$ 23 °/min (Figure 4g). The polar plot in Figure 4h is the real-time turning angle during the entire process and demonstrates that the robot can turn to a specific direction on demand by simply modulating the laser polarization and on-off switch.

If the robot is continuously driven by an x-polarized laser, it is possible to make a U-turn that has a turning angle of 180°. This simple extension of turning operation provides an effective approach toward backward moving. The design of the U-turn of the robot is illustrated in **Figure 5a**, with the same working principle as rightward turning. During 18 laser on-off cycles, we can observe a gradual change of robot heading from 0° to -45°, -90°, -135°, and finally -180° (Figure 5b). The transition is steady and even with an apparent angular velocity of ~27°/min (Figure 5c). It is highly possible to further enhance this angular velocity by increasing laser power density. The U-turn can be better shown by the real-time trajectory mapping of the A-wing of the robot (Figure 5d). As the robot makes a U-turn, point A is expected to follow a semicircular path, which is also confirmed by the real-time position changes of point A in experimental measurements.

In summary, we have developed a free-standing, multi-directional robot by simply modulating the polarization and on-off switch of a single laser. This new conceptual design is enabled by the confined growth of hybrid Fe<sub>3</sub>O<sub>4</sub>/Ag nanorods with a polymer shell. Due to the coupled magnetic-plasmonic anisotropy, the hybrid rods can be collectively aligned along specific directions in solution and solid film by applying a magnetic field. We have demonstrated that the plasmonic excitation and photothermal conversion properties of the nanorods can be modulated by magnetically controlling their orientation. Incorporating the nanorods into photo-curable polymers enables the construction of actuators whose mechanical bending can be controlled by switching laser polarization. By simply combining the polarization-dependent properties of hybrid nanorods into a bipedal robot, we have demonstrated the four fundamental movements of a robot. The unique properties of the magnetic/plasmonic hybrid nanorods enable the peculiar design of the bipedal robot, making it possible to overcome the restrictions on the existing photoactuators, such as the complicated actuation processes, high requirements for light sources, and limited actuation modes. The strategy of selective excitation of plasmonic modes by magnetic means can be used to create more functional materials and advanced devices, including not only next-generation self-sustained actuators and untethered robots but also high-performance colorimetric sensors, smart bioimaging contrast agents, active displays, and many other smart optical devices.

### **Supporting Information**

Supporting Information is available from the Wiley Online Library or from the author.

## Acknowledgements

The authors are grateful for the financial support from the U.S. National Science Foundation (CHE-1808788). The electron tomography work done at UCI is supported by the U.S. National Science Foundation (CHE-1900401). Myung and Yin are members of the UC-KIMS Center for Innovation

Materials for Energy and Environment jointly supported by UC Riverside and Korea Institute of Materials Science. This research used resources of the Center for Functional Nanomaterials, which is a U.S. DOE Office of Science Facility, at Brookhaven National Laboratory under Contract No. DE-SC0012704.

Received: ((will be filled in by the editorial staff))

Revised: ((will be filled in by the editorial staff))

Published online: ((will be filled in by the editorial staff))

### References

- [1] a) J. Deng, J. Li, P. Chen, X. Fang, X. Sun, Y. Jiang, W. Weng, B. Wang, H. Peng, J. Am. Chem. Soc. 2016, 138, 225; b) B. Han, Y. L. Zhang, Q. D. Chen, H. B. Sun, Adv. Funct. Mater. 2018, 28, 1802235; c) X. Zhang, Z. Yu, C. Wang, D. Zarrouk, J.-W. T. Seo, J. C. Cheng, A. D. Buchan, K. Takei, Y. Zhao, J. W. Ager, Nat. Commun. 2014, 5, 1.
- [2] a) J. Chen, J. Feng, F. Yang, R. Aleisa, Q. Zhang, Y. Yin, *Angew. Chem.* 2019, *131*, 9376;
  b) Q. Shi, H. Xia, P. Li, Y. S. Wang, L. Wang, S. X. Li, G. Wang, C. Lv, L. G. Niu, H. B. Sun, *Adv. Opt. Mater.* 2017, *5*, 1700442; c) Z. Li, W. Wang, Y. Yin, *Trends Chem.* 2020.
- [3] A. H. Gelebart, D. J. Mulder, G. Vantomme, A. P. Schenning, D. J. Broer, *Angew. Chem. Int. Ed.* **2017**, *56*, 13436.
- [4] Z. Li, F. Yang, Y. Yin, Adv. Funct. Mater. 2020, 30, 1903467.
- [5] a) S. Yao, J. Cui, Z. Cui, Y. Zhu, Nanoscale 2017, 9, 3797; b) M. Acerce, E. K. Akdoğan,
   M. Chhowalla, Nature 2017, 549, 370.
- [6] X. Zhao, Y. Kim, Nature Publishing Group, **2019**.
- [7] a) Y. Wang, H. Cui, Q. Zhao, X. Du, Matter 2019, 1, 626; b) Z. Li, Y. Yin, Matter 2019, 1, 550.

- [8] a) W. Wang, C. Xiang, D. Sun, M. Li, K. Yan, D. Wang, ACS applied materials & interfaces 2019, 11, 21926; b) H. Arazoe, D. Miyajima, K. Akaike, F. Araoka, E. Sato, T. Hikima, M. Kawamoto, T. Aida, Nature Mater. 2016, 15, 1084.
- [9] X. Du, H. Cui, Q. Zhao, J. Wang, H. Chen, Y. Wang, Research 2019, 2019, 6398296.
- [10] X. Zhang, C. L. Pint, M. H. Lee, B. E. Schubert, A. Jamshidi, K. Takei, H. Ko, A. Gillies,R. Bardhan, J. J. Urban, *Nano Lett.* 2011, *11*, 3239.
- [11] Z. Li, Y. Yin, Adv. Mater. **2019**, *31*, 1807061.
- [12] a) S. Iamsaard, S. J. Aßhoff, B. Matt, T. Kudernac, J. J. Cornelissen, S. P. Fletcher, N. Katsonis, *Nature chemistry* 2014, 6, 229; b) G. L. Liu, J. Kim, Y. Lu, L. P. Lee, *Nature Mater.* 2006, 5, 27; c) D. D. Han, Y. L. Zhang, J. N. Ma, Y. Q. Liu, B. Han, H. B. Sun, *Adv. Mater.* 2016, 28, 8328.
- [13] a) T. Wang, D. Torres, F. E. Fernández, C. Wang, N. Sepúlveda, *Sci. Adv.* 2017, 3, e1602697; b) L. Hines, K. Petersen, G. Z. Lum, M. Sitti, *Adv. Mater.* 2017, 29, 1603483;
  c) H. Ko, A. Javey, *Acc. Chem. Res.* 2017, 50, 691; d) D. Chen, Q. Pei, *Chem. Rev.* 2017, 117, 11239.
- [14] a) T. Lan, Y. Hu, G. Wu, X. Tao, W. Chen, J. Mater. Chem. C 2015, 3, 1888; b) M. Lahikainen, H. Zeng, A. Priimagi, Nat. Commun. 2018, 9, 1; c) H. Lim, T. Park, J. Na, C. Park, B. Kim, E. Kim, NPG Asia Materials 2017, 9, e399; d) X. Lu, H. Zhang, G. Fei, B. Yu, X. Tong, H. Xia, Y. Zhao, Adv. Mater. 2018, 30, 1706597.
- [15] W. Fan, C. Shan, H. Guo, J. Sang, R. Wang, R. Zheng, K. Sui, Z. Nie, *Sci. Adv.* **2019**, *5*, eaav7174.
- [16] S. Maeda, Y. Hara, T. Sakai, R. Yoshida, S. Hashimoto, *Adv. Mater.* **2007**, *19*, 3480.

- [17] Y. Dong, J. Wang, X. Guo, S. Yang, M. O. Ozen, P. Chen, X. Liu, W. Du, F. Xiao, U. Demirci, *Nat. Commun.* **2019**, *10*, 1.
- [18] Z. Sun, Y. Yamauchi, F. Araoka, Y. S. Kim, J. Bergueiro, Y. Ishida, Y. Ebina, T. Sasaki,T. Hikima, T. Aida, *Angew. Chem.* 2018, 130, 15998.
- [19] B. Zuo, M. Wang, B.-P. Lin, H. Yang, Nat. Commun. 2019, 10, 1.
- [20] a) D. Martella, S. Nocentini, F. Micheletti, D. S. Wiersma, C. Parmeggiani, Soft Matter
  2019, 15, 1312; b) A. W. Hauser, D. Liu, K. C. Bryson, R. C. Hayward, D. J. Broer,
  Macromolecules 2016, 49, 1575.
- [21] Z. Li, J. Jin, F. Yang, N. Song, Y. Yin, *Nat. Commun.* **2020**, *11*, 1.
- [22] a) Z. Li, M. Wang, X. Zhang, D. Wang, W. Xu, Y. Yin, Nano Lett. 2019, 19, 6673; b) W.
   Xu, M. Wang, Z. Li, X. Wang, Y. Wang, M. Xing, Y. Yin, Nano Lett. 2017, 17, 2713.
- [23] Z. Li, S. Yin, L. Cheng, K. Yang, Y. Li, Z. Liu, Adv. Funct. Mater. 2014, 24, 2312.
- [24] C. Gao, Y. Hu, M. Wang, M. Chi, Y. Yin, J. Am. Chem. Soc. 2014, 136, 7474.
- [25] a) B. Pietrobon, M. McEachran, V. Kitaev, ACS nano 2009, 3, 21; b) C. Gao, Q. Zhang,Z. Lu, Y. Yin, J. Am. Chem. Soc. 2011, 133, 19706.
- [26] Y. Yin, A. P. Alivisatos, *Nature* **2005**, *437*, 664.
- [27] Q. Zhang, Y. Hu, S. Guo, J. Goebl, Y. Yin, *Nano Lett.* **2010**, *10*, 5037.
- [28] M. Xing, B. Chen, J. Feng, W. Xu, Y. Bai, Y. Zhou, C. Dong, H. Zhong, J. Zhang, Y. Yin, Chem 2019, 5, 2195.
- [29] a) M. Wang, C. Gao, L. He, Q. Lu, J. Zhang, C. Tang, S. Zorba, Y. Yin, J. Am. Chem. Soc. 2013, 135, 15302; b) L. Wu, M. Ohtani, M. Takata, A. Saeki, S. Seki, Y. Ishida, T. Aida, ACS nano 2014, 8, 4640; c) X. Wang, X. Li, S. Aya, F. Araoka, Y. Ishida, A. Kikkawa, M. Kriener, Y. Taguchi, Y. Ebina, T. Sasaki, J. Am. Chem. Soc. 2018, 140,

- 16396; d) M. Liu, Y. Ishida, Y. Ebina, T. Sasaki, T. Hikima, M. Takata, T. Aida, *Nature* **2015**, *517*, 68.
- [30] M. Wang, Y. Yin, J. Am. Chem. Soc. 2016, 138, 6315.
- [31] a) T. Ming, L. Zhao, Z. Yang, H. Chen, L. Sun, J. Wang, C. Yan, *Nano Lett.* 2009, 9, 3896; b) J. Kim, J. Peretti, K. Lahlil, J. P. Boilot, T. Gacoin, *Adv. Mater.* 2013, 25, 3295;
  c) J.-M. Lamarre, F. Billard, C. H. Kerboua, M. Lequime, S. Roorda, L. Martinu, *Opt. Commun.* 2008, 281, 331; d) M. J. Hore, R. J. Composto, *ACS nano* 2010, 4, 6941.
- [32] a) M. H. Madsen, N. A. Feidenhans, P.-E. Hansen, J. Garnæs, K. Dirscherl, Journal of Micromechanics and Microengineering 2014, 24, 127002; b) C. Goldsmith, P. Geldermans, F. Bedetti, G. Walker, Journal of Vacuum Science & Technology A: Vacuum, Surfaces, and Films 1983, 1, 407.

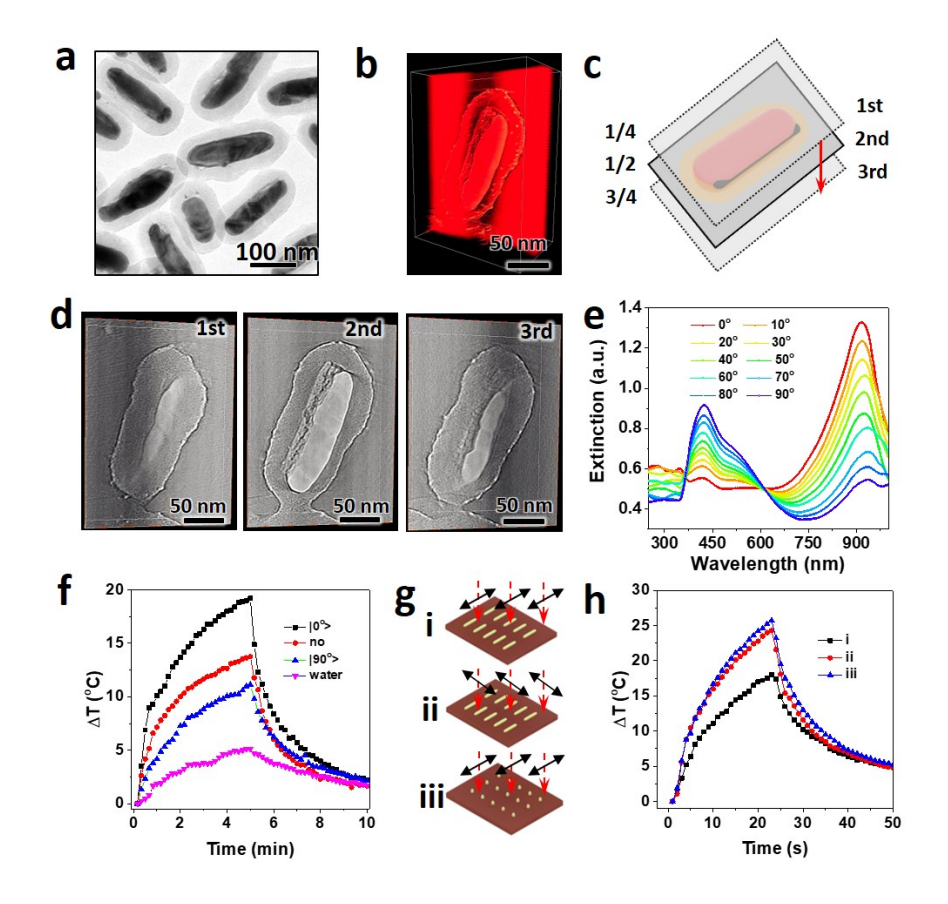


**Figure 1.** a) TEM image of the hybrid Fe<sub>3</sub>O<sub>4</sub>/Ag@RF nanorods. b) The 3D reconstruction of the hybrid nanorods after electron tomography. c) Schematic illustration of the slicing of a hybrid Fe<sub>3</sub>O<sub>4</sub>-Ag nanorod in electron tomography. d) Horizontal slices at three vertical positions from the reconstructed tomogram of an individual hybrid rod. e) Extinction spectra of hybrid nanorods in a colloidal dispersion by changing the magnetic field directions. The spectra were measured under polarized light. f) Temperature changes of the colloidal dispersion of hybrid nanorods under different magnetic field directions and 450-nm laser irradiation. g) Scheme showing the alignment of hybrid nanorods in polymer films for photothermal measurement. h) Temperature increases in the polymer films under 450-nm laser irradiation.

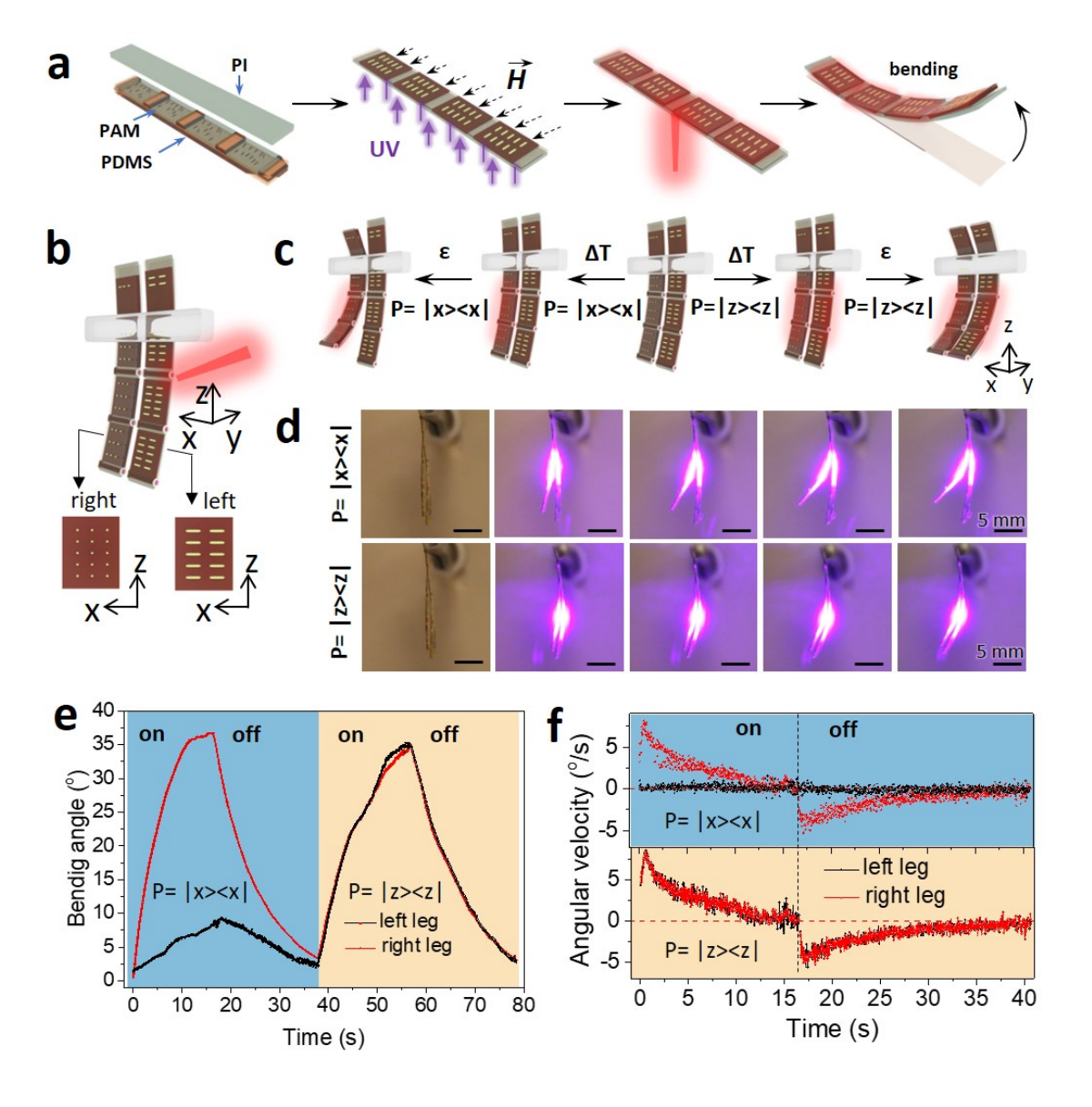


**Figure 2.** a) Fabrication of the photothermal actuators and the polarization-dependent bending. b) Schematic illustration of the rod alignment in the photothermal robots. c) Schematic illustration of the selective actuation of the two legs of the robot by changing the polarization of a 450-nm laser. d) Photographs of the robot actuated by a x-polarized (up panel) and z-polarized laser (bottom panel). The real-time bending angle (e) and angular velocity (f) of the two legs of the robot actuated under x-polarized and z-polarized laser.

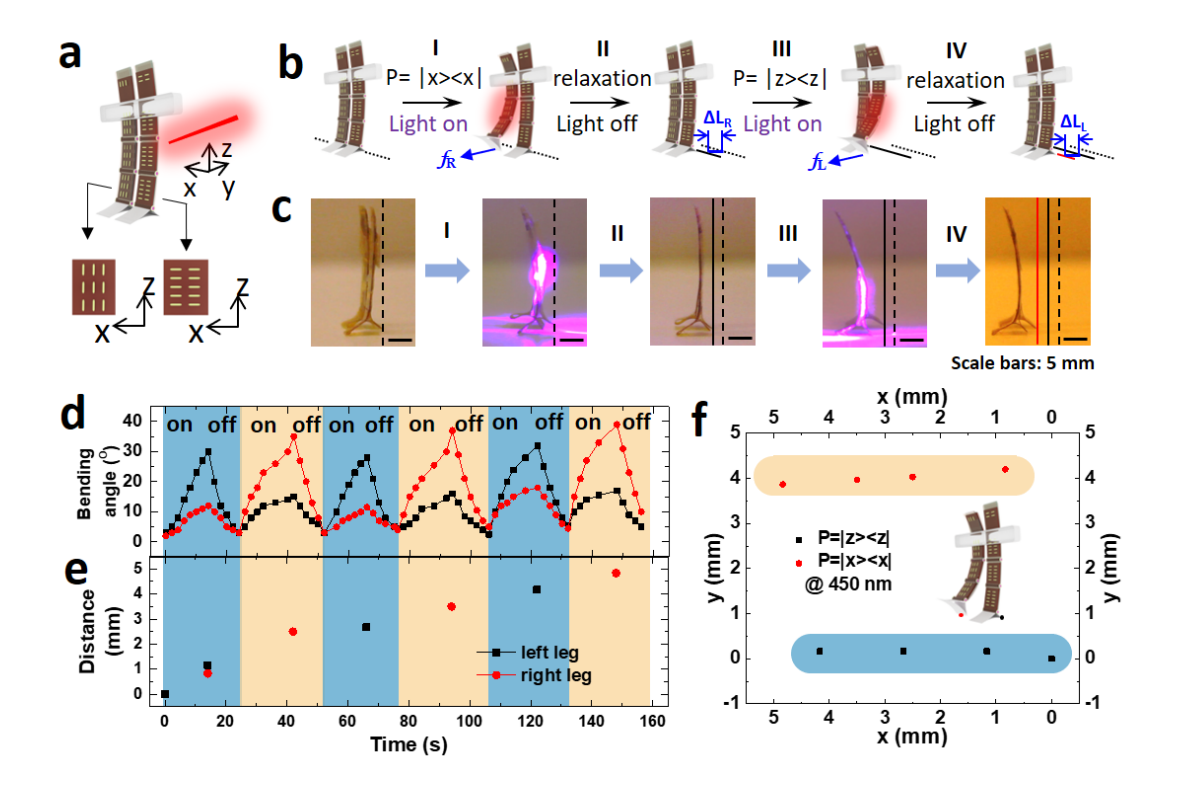


**Figure 3.** a) Schematic illustration of the rod alignment in the two legs of the robot. b) Schematic illustration of the step-to-step walking dynamics of the free-standing robot. c) Photographs showing the stepping of the robot during the cooperative actuation of the two legs by switching the polarization of the laser. The real-time bending angle (d) and moving distance (e) of the two legs. (f) The real-time position coordination of the middle point of the two legs.

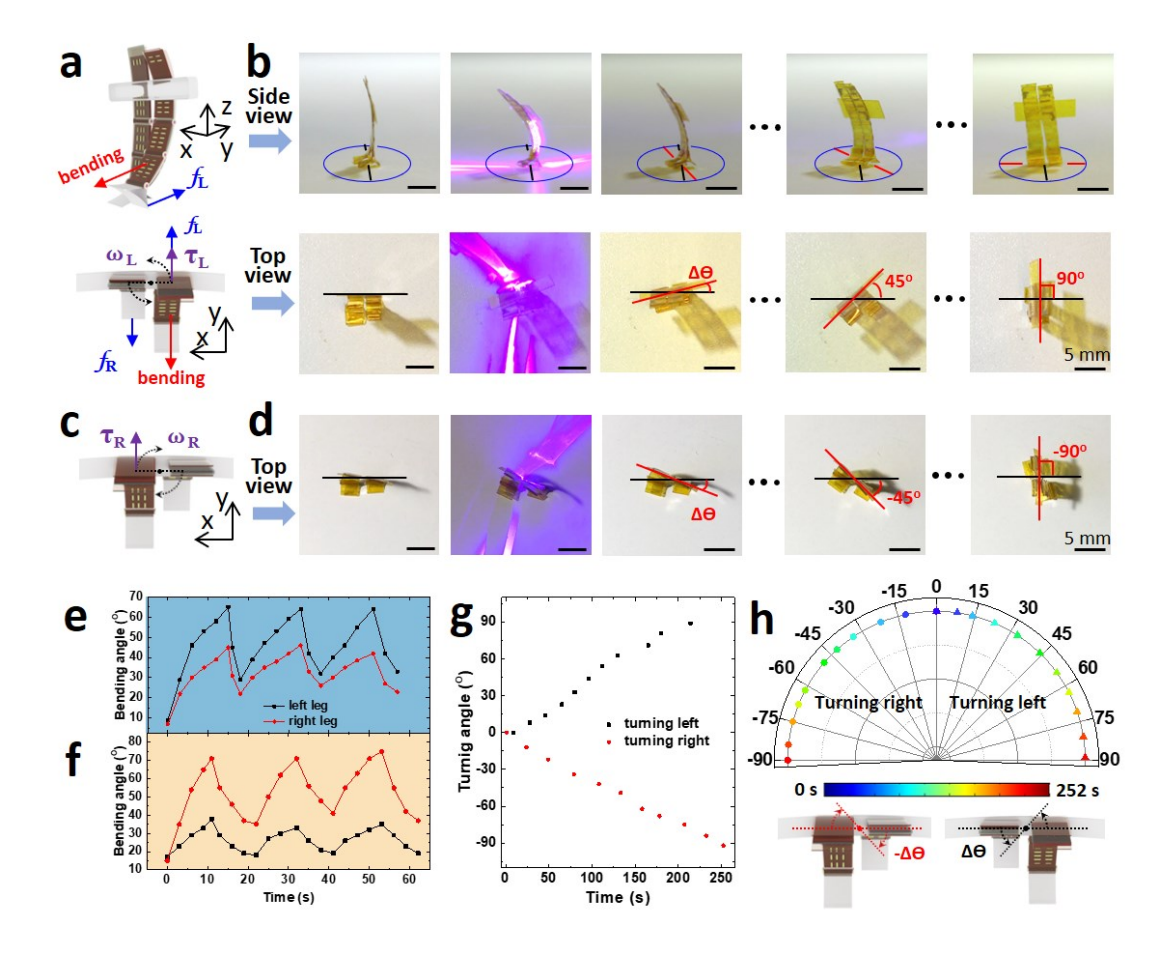


**Figure 4.** a) Schematic illustration of the left-turning mechanism and the force analysis of the free-standing robot when actuated by a z-polarized light. b) The photographs of the left-turning of the free-standing robot. The side view and the top view are shown in the up and bottom panels, respectively. c) Schematic illustration of the right-turning of the robot powered by the x-polarized laser. d) The top-view photographs of the right-turning of the robot. The real-time bending angle of the two legs under (e) z-polarized and (f) x-polarized light. g) The real-time turning angles of the robot. h) Polar plot of the turning angles of the robot. The insets show the definition of the tuning angles during right- and left-turning.

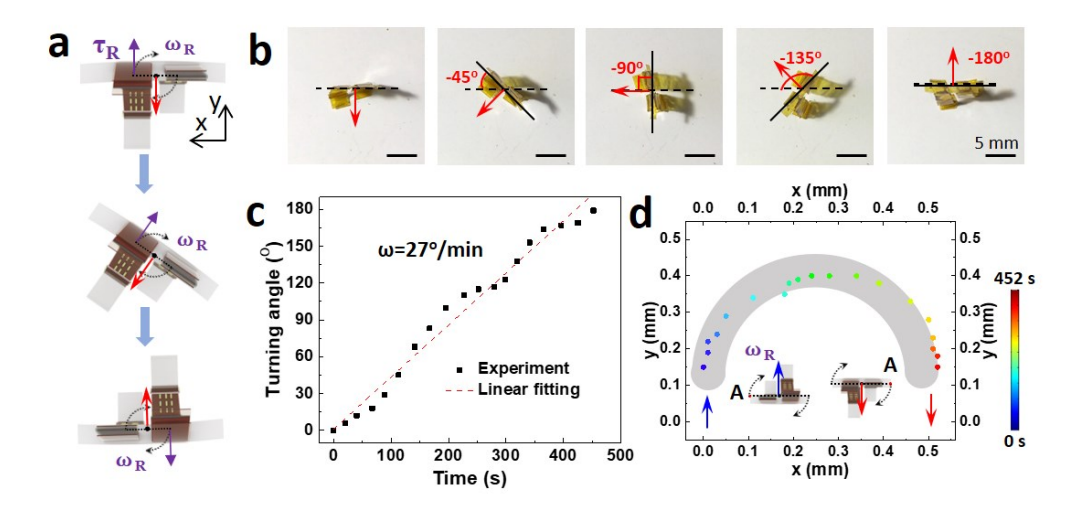


**Figure 5.** a) Schematic illustration of the U-turn mechanism of the free-standing robot when actuated by a z-polarized light. b) The top-view photographs of the U-turn of the free-standing robot. c) The real-time turning angles of the robot. d) The real-time position coordinates of the point "A" in the U-turn of the robot. Reds arrow indicate the robot heading.